

Strategically Designed Mitochondria-Targeting AIEgens for Effective Eradication of Primary and Metastatic Tumors via Synergistic Phototherapy and Induced Immunogenic Cell Death

Lin Yang, Jiachang Huang, Yanan Liao, Deping Hu, Yake He, Na Feng, Ryan T. K. Kwok, Jacky W. Y. Lam, Jing Zhang,* Benzhao He,* and Ben Zhong Tang**

In recent years, photoimmunotherapy has emerged as an innovative modality in antitumor therapy, garnering significant research interest due to its integration of the advantages of both phototherapy and immunotherapy. However, despite extensive efforts to advance photoimmunotherapy, the design strategies for photoimmunotherapy agents remain uncertain, significantly hindering progress in this field. Here, a novel molecular design strategy for developing superb photoimmunotherapy agents that integrates aggregation-induced emission (AIE) activity, mitochondria targeting, high-efficiency reactive oxygen species generation, and high photothermal conversion capabilities into a single molecule is proposed. A comprehensive study demonstrates that the target molecule (TPETTBI) that is strategically designed can exert prominent photodynamic therapy (PDT) and photothermal therapy (PTT) effects, leading to tumor cell death. More importantly, the synergistic action of PDT and PTT can further induce mitochondrial dysfunction and trigger large-scale immunogenic cell death (ICD) to attain a long-lasting effect of antitumor immunity. Therefore, this work provides new insights into the rational design of phototherapy agents for precise and efficient tumor treatment by integrating synergistic PDT, PTT, and ICD-based immunotherapy within a single molecule.

1. Introduction

Cancer remains a significant threat to human health and poses a major worldwide health challenge.^[1] Over the past century, a diverse array of therapeutic strategies, such as chemotherapy and radiation therapy, have been developed to combat cancer. However, the high toxicity and limited tolerance of these methods have restricted their clinical application and further development.^[2,3] Antitumor immunotherapy, which harness the body's immune response against tumors, has shown promising clinical outcomes.^[4] In contrast to conventional treatment modalities, immunotherapy has the potential to induce systemic antitumor effects, particularly in targeting abscopal tumors that are often difficult to treat.^[5–7] Nevertheless, only a small proportion of patients respond to immunotherapy, primarily due to the complexity of the tumor microenvironment and tumors' low immunogenicity.^[8,9]

L. Yang, Y. Liao, N. Feng, J. Zhang

Department of Laboratory Medicine

Guangdong Provincial Key Laboratory of Precision Medical Diagnostics

Guangdong Engineering and Technology Research Center for Rapid

Diagnostic Biosensors Guangdong Provincial Key Laboratory of

Single-cell and Extracellular Vesicles

Nanfang Hospital

Southern Medical University

Guangzhou 510515, China

E-mail: zjsilence@i.smu.edu.cn

J. Huang, D. Hu, Y. He, B. He

Center for Advanced Materials Research

Faculty of Arts and Sciences

Instrumentation and Service Center for Science and Technology

Beijing Normal University

Zhuhai 519085, China

E-mail: hebenzhao@bnu.edu.cn

R. T. K. Kwok, J. W. Y. Lam

Department of Chemistry

Hong Kong Branch of Chinese National Engineering Research Center for Tissue Restoration and Reconstruction

Department of Chemical and Biological Engineering

State Key Laboratory of Molecular Neuroscience

Division of Life Science

The Hong Kong University of Science and Technology

Clear Water Bay, Kowloon, Hong Kong 999077, China

E-mail: chjacky@ust.hk

B. Z. Tang

School of Science and Engineering

Shenzhen Institute of Aggregate Science and Technology

The Chinese University of Hong Kong

Shenzhen (CUHK-Shenzhen), Guangdong 518172, China

E-mail: tangbenz@cuhk.edu.cn

 The ORCID identification number(s) for the author(s) of this article can be found under <https://doi.org/10.1002/adhm.202500513>

DOI: 10.1002/adhm.202500513

Notably, immunogenic cancer cell death (ICD), as a form of cell death that activates the innate immune system to eliminate cancer cells and maintain long-term immunological vigilance, has emerged as a particularly effective immunostimulatory mechanism with potential to reshape the tumor microenvironment and enhance immunogenicity, thereby initiating systemic antitumor immunity.^[10–12]

Since the elucidation of the ICD mechanism, ICD-based antitumor therapies have garnered significant research interest.^[13–16] Among them, phototherapy induced immunotherapy stands out as a superior strategy for its non-invasive nature, high temporal and spatial precision and minimum toxic side effect. Phototherapy includes photodynamic therapy (PDT) and photothermal therapy (PTT).^[17] Studies have demonstrated that reactive oxygen species (ROS) generated in PDT can trigger ICD by causing oxidative stress in tumor cells, whereas PTT can effectively destroy tumor cells, promoting the release of tumor-associated antigens and thus enhancing the ICD effect.^[18] Consequently, the combination of PDT and PTT can synergistically amplify the ICD response.

Although the synergistic effects of PDT and PTT are regarded as a promising modality in antitumor therapy, certain limitations still exist. On one hand, according to the Jablonski diagram, the heat and ROS generation process are considered as two competitive pathways during the nonradiative decay.^[19] Furthermore, the generated ROS display a limited lifespan, which result in an extremely short diffusion distance. Therefore, the efficient use of the produced heat and ROS is very critical for treatment, and precise and specific organelle targeting is an effective way to enhance the availability of these two factors to exert efficient anti-cancer.^[20] Mitochondria, known as “powerhouses of the cell”, are involved in numerous physiological processes.^[21,22] As critical organelle, mitochondria are promising targets for tumor therapy.^[23] Most importantly, mitochondria exhibit a heightened sensitivity to ROS and heat, which means mitochondria-targeting phototherapy agents may potentially possess better phototherapy efficiency.^[3,24–26] On the other hand, the production capabilities of heat and ROS for the photosensitizer itself play a decisive role in the therapeutic effect. It is worth noting that most of conventional photosensitizers are prone to aggregation in physiological environments, leading to intermolecular interactions (e.g., π - π stacking) as a result of their hydrophobic nature and planar structure, which reduces fluorescence emission and limits ROS generation, ultimately impeding effective ICD induction.^[27,28] Aggregation-induced emission luminogens (AIEgens), as a special class of photosensitizers,^[29–31] have demonstrated particularly prominent generation abilities of both heat and ROS.^[32–34] The formation of their aggregates can greatly promote both the radiative and non-radiative decay processes, thus favoring the generation of heat and intersystem crossing (ISC)-associated ROS. Therefore, AIE-active phototherapy agents offer advantages over traditional photosensitizers in both fluorescence imaging-guided phototherapy and increased phototherapy efficiency in the aggregated state.^[29,35] Accordingly, AIEgens emerge as promising candidates for superior ICD induction.

Besides, phototherapy, as a photon-driven therapy, is heavily dependent on the light source. However, the restricted penetration of light significantly limits the efficiency of this therapy

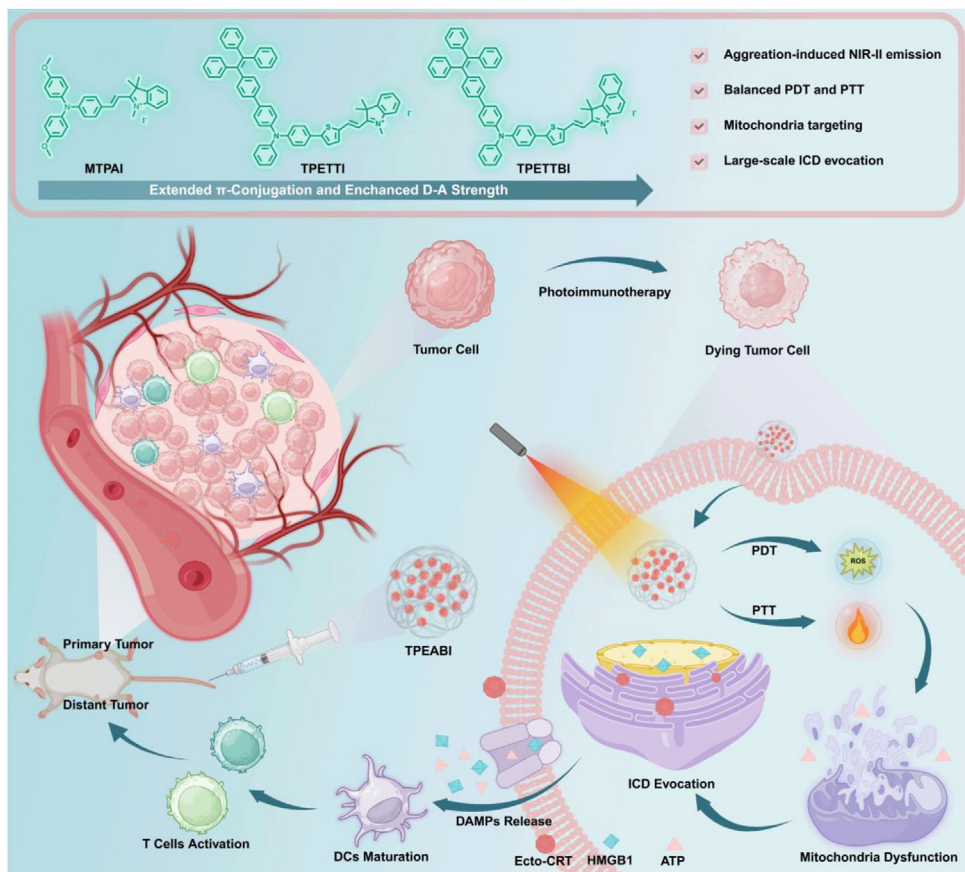
approach.^[36,37] Compared to visible light, near-infrared light offers superior tissue penetration and lower toxicity. Additionally, near-infrared (NIR) fluorescence emission facilitates real-time imaging and monitoring, which is essential for minimizing collateral damage to normal tissue and reducing the risk of adverse side effects.^[38–40] Taken the above factors together, developing novel AIEgens with mitochondria-targeting, high-efficiency PDT, and PTT capabilities, as well as NIR excitation or emission wavelengths, hold promise for enhancing efficiency, accuracy, and ultimately promoting effective ICD induction during phototherapy.

Despite extensive efforts to explore ICD-based antitumor therapies, the design strategy for phototherapy agents that evoke ICD remains uncertain, often relying on a “trial-and-error” approach, which significantly hinders the progress in photoimmunotherapy (PIT). In this regard, we propose combining typical AIE-active triphenylamine (TPA) structure with indolium moiety that possess native mitochondria targeting ability to construct donor-acceptor (D-A) type of phototherapy agents and work as superior ICD inducers. Through molecular engineering, the D-A and conjugation degrees were elaborately modulated to achieve enhanced ROS generation, improved photothermal conversion efficiency and long-wavelength NIR emission. Herein, a series of new AIEgens, named MTPAI, TPETTI, and TPETTB1, with increased donor-acceptor strength and conjugation degree was synthesized in this work. Among them, TPETTB1 with the strongest D-A strength and the most twisted structure demonstrated superior mitochondrial-targeting ability, optimal ROS generation and photothermal conversion efficiency. These features contributed to an enhanced tumor suppression and ICD induction, thus activating durable anti-tumor immune memory and effectively suppressing metastatic distal tumors in mouse models (**Scheme 1**). Therefore, this study provides new insights into the rational design of photosensitizers for efficient, sustained, and safe tumor treatment through the synergistic application of PDT, PTT, and ICD-based immunotherapy within a single small molecule.

2. Results and Discussion

2.1. Molecular Design and Synthesis

Strong electron donor and acceptor groups can enhance the absorption and emission properties of fluorophores and the establishment of a D-A system further promotes the generation of ROS. The indolium group, recognized for its strong electron accepting properties, has been widely used to improve both the absorption and emission characteristic of fluorophores. Fluorophores containing indolium structure typically localized in mitochondria due to their zwitterionic nature.^[24] Therefore, this study aimed to introduce the indolium group to improve both the absorption and emission capabilities, as well as the mitochondria-targeting ability of the fluorophores. In the primarily designed molecule, MTPAI, 4,4'-dimethoxytriphenylamine was selected as the AIE unit and donor unit, which is connected to the acceptor unit via a double bond. To further improve the AIE property and achieve a red-shifted emission wavelength, TPETTI incorporated additional rotatable unit and an extended π -conjugation system. Furthermore, to enhance the absorption of the target molecule, 1,1,2-trimethyl-1*H*-benz[e]indole was introduced. This modification could provide the highest D-A



Scheme 1. Schematic illustration of the molecular design strategy of TPETTBI and its application in photoimmunotherapy within a bilateral 4T1 tumor-bearing mouse model. Created in BioRender. <https://Biorender.com/77vmphn>. After the intravenous administration of TPETTBI nanoparticles, abundant amount of TPETTBI can be accumulated in the tumor site. Once internalized by tumor cells, TPETTBI targets the mitochondria, where excessive reactive oxygen species (ROS) generated under laser irradiation causes mitochondrial dysfunction and promote the generation of damage-associated molecular patterns (DAMPs). In the meantime, the photothermal effect of TPETTBI facilitated the release of DAMPs. Consequently, the synergistic photodynamic therapy (PDT) and photothermal therapy (PTT) effect mediated by TPETTBI effectively induces large-scale immunogenic cell death (ICD). The released DAMPs from the primary tumor cells including adenosine triphosphate (ATP), high-mobility group box 1 (HMGB1), and surface-exposed calreticulin (ecto-CRT) can activate a cascade of antitumor immune responses, prompting the maturation of dendritic cells (DCs) and the infiltration of activated T cells in the untreated distant tumor, and eventually leads to the inhabitation of bilateral tumor.

intensity, potentially achieving the longest emission wavelength. Accordingly, three new D-A type compounds with different D-A strength and conjugation degree were designed and synthesized. The structure of the three compounds were confirmed through nuclear magnetic resonance (NMR) spectra and high-resolution mass spectrometry (HRMS) (Figures S1–S9, Supporting Information).

2.2. Photophysical Properties of MTPAI, TPETTI, and TPETTBI

The photophysical properties of the compounds were systematically investigated. As shown in Figure 1a, MTPAI, TPETTI, and TPETTBI exhibited strong absorption at 540, 567, and 576 nm, respectively. As anticipated, TPETTI and TPETTBI, which feature extended π -conjugation, exhibited longer absorption profiles. Among them, TPETTBI demonstrated the highest molar absorption coefficient, measuring $4.6 \times 10^4 \text{ M}^{-1} \text{ cm}^{-1}$ (Figure S10, Supporting Information). Notably, portions of absorption

profiles of TPETTI and TPETTBI fall within the biological tissue transparency window (650–950 nm),^[38] which suggests their considerable potential for deep tissue theranostic application. The emission wavelengths of them reflected a gradual extended trend, from MTPAI to TPETTI and TPETTBI (Figure 1b). This ordering can be attributed to the extended π -conjugation and the enhanced D-A strength of TPETTI and TPETTBI. Importantly, the emission spectra of TPETTI and TPETTBI extend into the near-infrared region, potentially offering enhanced compatibility for in vivo imaging. Subsequently, the AIE properties of these three compounds were investigated in DMSO/H₂O mixtures. As illustrated in Figure 1c, the emission intensities of both TPETTI and TPETTBI were enhanced with the increasing fraction of water, demonstrating typical AIE characteristics (Figure S11, Supporting Information).

To evaluate the overall photoinduced ROS generation ability, 2',7'-dichlorodihydrofluorescein diacetate (DCFH-DA) was used as the indicator (Figure 1d; Figure S12, Supporting Information). Under light irradiation, the fluorescence of DCFH showed no

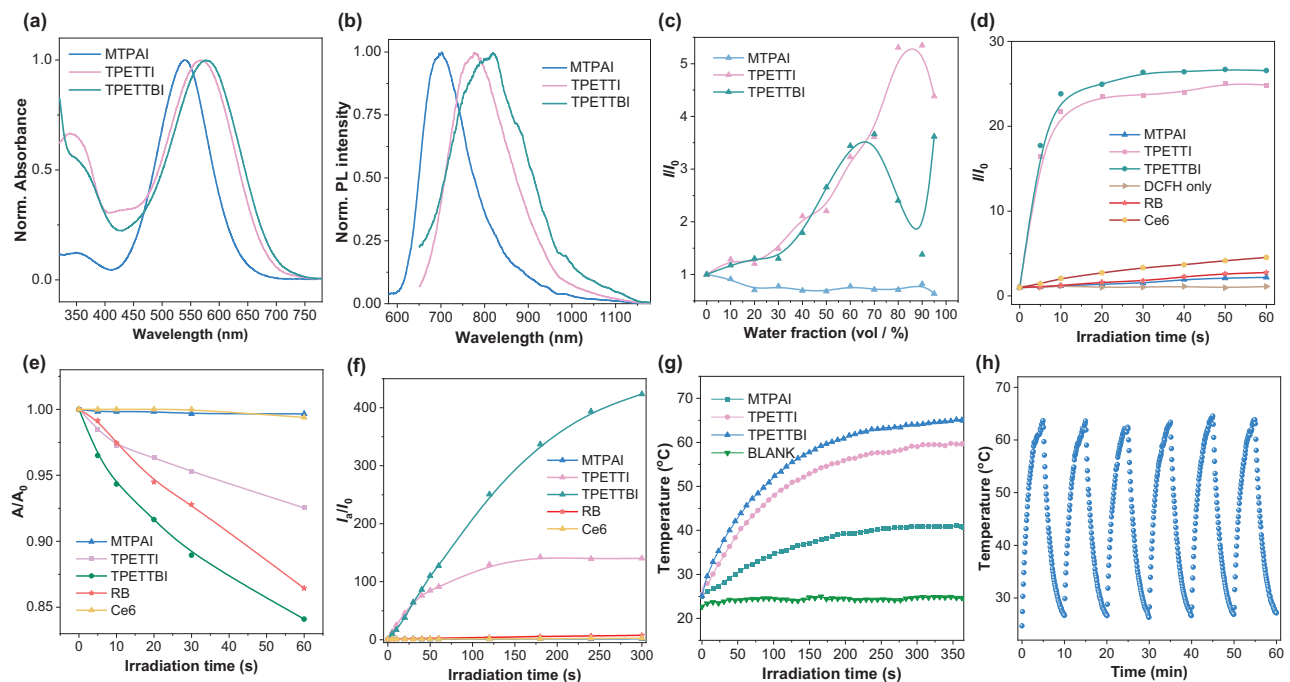


Figure 1. Characterization of three resulted compounds. Normalized a) absorption and b) PL spectra of MTPAI, TPETTI and TPETTB in DMSO. c) Plot of peak PL intensity versus water fraction of DMSO/water mixture for MTPAI, TPETTI and TPETTB. (I = PL intensity, I_0 = PL intensity in DMSO). Changes in d) DCHF fluorescence, e) ABDA absorbance, and f) DHR123 fluorescence in the presence of various agents upon irradiation. g) Temperature elevation profile of different agents (0.2 mM) under 660 nm laser irradiation (0.4 W cm⁻²). h) The curve of temperature change of TPETTB (0.2 mM) under repeated laser irradiation (0.4 W cm⁻²) and cooling cycles.

significant change, while a gradual increase in fluorescence was observed in the presence of MTPAI. In the case of TPETTB, fluorescence increased under irradiation and reached a plateau within 10 s. The TPETTI group showed similar changes. These results indicate the superior ROS generation abilities of both TPETTI and TPETTB. Notably, the ROS generation abilities of TPETTB and TPETTI were found to be superior to those of the commercial photosensitizers, such as Rose Bengal (RB) and Ce6. To identify the specific ROS species generated, anthracenediyl-bis(methylene) dimalonic acid (ABDA) (Figure 1e; Figure S13, Supporting Information) and dihydrorhodamine 123 (DHR123) (Figure 1f; Figure S14, Supporting Information) were utilized to detect the generation of singlet oxygen ($^1\text{O}_2$) and superoxide ($\text{O}_2^{\bullet-}$), respectively. The absorption of ABDA at 378 nm exhibited a sharp decline in the presence of TPETTI, TPETTB, and RB, respectively, demonstrating their abilities to generate $^1\text{O}_2$ via the type II photochemical pathway. The emission intensities of DHR123 at 526 nm increased drastically in the presence of TPETTI (140.3-fold) and TPETTB (423.5-fold), respectively, compared to those of non-irradiation. In contrast, weak and negligible changes in emission intensities were observed in the MTPAI group. The results demonstrate that TPETTI and TPETTB can effectively generate both type I and type II ROS, as well as superior overall ROS generation compared to RB and Ce6. The photothermal behaviors of the three compounds were also assessed. As illustrated in Figure 1g, after irradiation with a 660 nm laser for 5 min, the temperature of MTPAI, TPETTI, and TPETTB drastically increased and reached plateaus at 40.9, 59.9, and 65.0 °C, respectively. Notably, TPETTB demonstrated the best photothermal performance and negligible temperature decay after six cycles of heating and cooling under a 660 nm laser (0.4 W cm⁻²) (Figure 1h). Therefore, the NIR-II emission, superior ROS generation ability, high photothermal efficiency and thermal stability make TPETTB as a promising candidate for theranostic applications.

thermal performance and negligible temperature decay after six cycles of heating and cooling under a 660 nm laser (0.4 W cm⁻²) (Figure 1h). Therefore, the NIR-II emission, superior ROS generation ability, high photothermal efficiency and thermal stability make TPETTB as a promising candidate for theranostic applications.

2.3. Mitochondria-Targeted and Wash-Free Imaging

After confirming the excellent photophysical properties of TPETTB, we further investigated its imaging ability at the cellular level. Commercial probes, including Dio (membrane probe), Lys-Tracker Green (LTG), and Mito-Tracker Green (MTG), were used to investigate the cellular localization of TPETTB. As shown in Figure 2a, the green fluorescence signals from MTG showed substantial overlap with the red fluorescence from TPETTB, whereas the red fluorescence signals from TPETTB did not overlap with signals from either LTG and Dio. Those results demonstrate the excellent mitochondria-targeting ability of TPETTB, which can be attributed to its zwitterionic structure. In addition, since mitochondria are promising targets for tumor therapy, the mitochondria-targeting ability of TPETTB may potentially enhance its phototherapy efficiency. Subsequently, time-dependent imaging was performed. As shown in Figure 2b, TPETTB was able to visualize the mitochondria within 10 min, and the fluorescence intensity gradually increased with the incubation time. Notably, throughout the process, the background signal remained negligible without washing. The fluorescence signal showed no

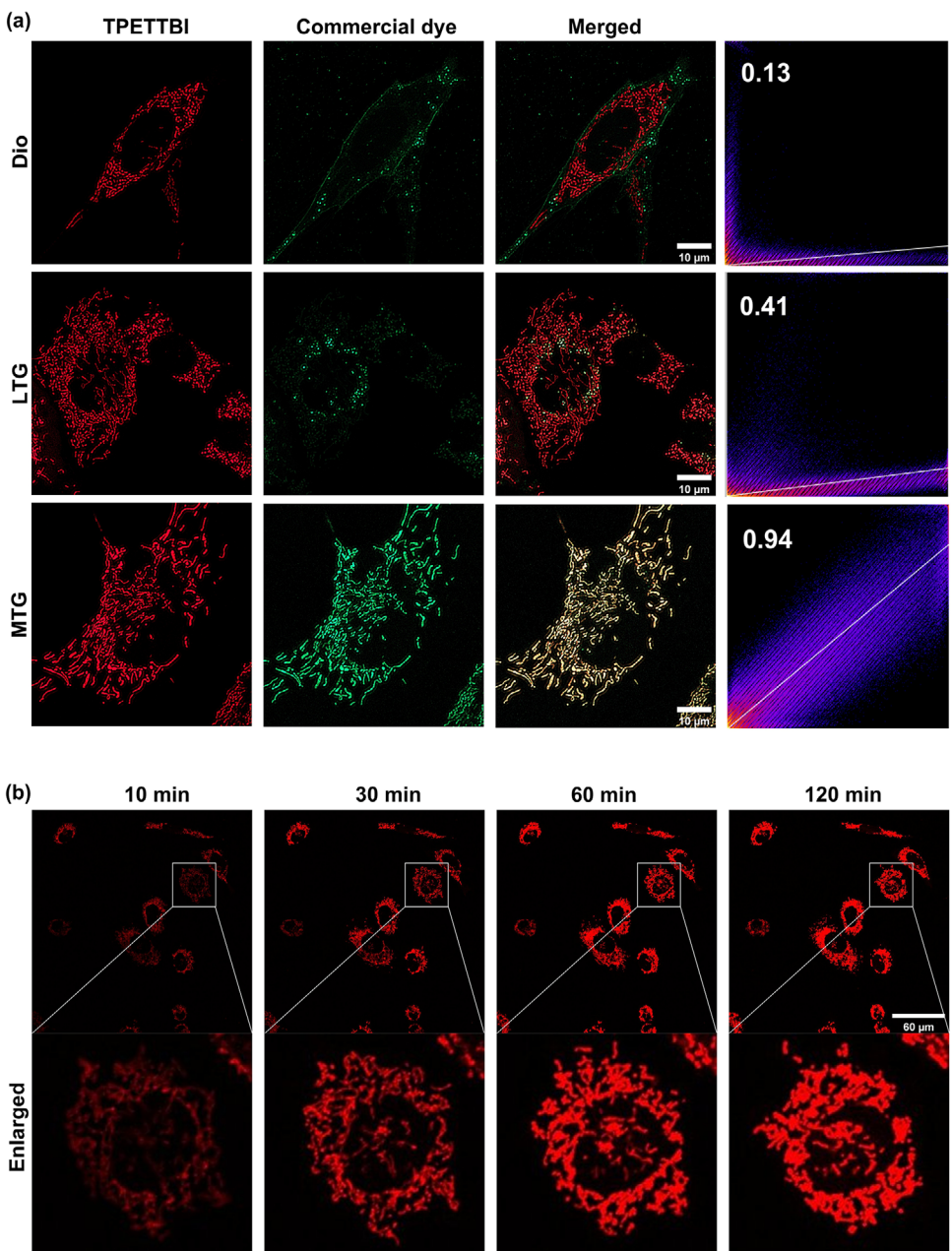


Figure 2. Cell staining performance study. a) Colocalization CLSM images of 4T1 cells stained by TPETTB1 (1 μM) and different commercial dyes including Dio, LTC, and MTG. Scale bar = 10 μm. b) Time-dependent CLSM images of 4T1 cells after addition of TPETTB1 in washing-free manner. Scale bar = 60 μm.

decay even after 3 h of continuous imaging, demonstrating the excellent photostability of TPETTB1 (Figure S15, Supporting Information). The ultrafast and wash-free staining ability can be attributed to the amphiphilic nature and AIE property of TPETTB1. On one hand, the lipophilic portion of TPETTB1 facilitates its easy uptake by cells. On the other hand, the positively charged moiety enables TPETTB1 to accumulate in the negatively charged mitochondria. Furthermore, the fluorescence intensity of TPETTB1 increased drastically after aggregation in the mitochondria, which can be explained by the restriction of intramolecular motion (RIM) mechanism in the AIE process.^[41] The turn-on flu-

orescence property of TPETTB1 increases the signal-to-noise ratio, revealing the great potential of TPETTB1 in high-resolution imaging of mitochondria.

2.4. In Vitro Tumoricidal Evaluation

Motivated by the superior photodynamic and photothermal efficacy, as well as the excellent mitochondria-targeting ability, the phototherapeutic performance of TPETTB1 was further evaluated. First, the dark toxicity and phototoxicity of TPETTB1 were

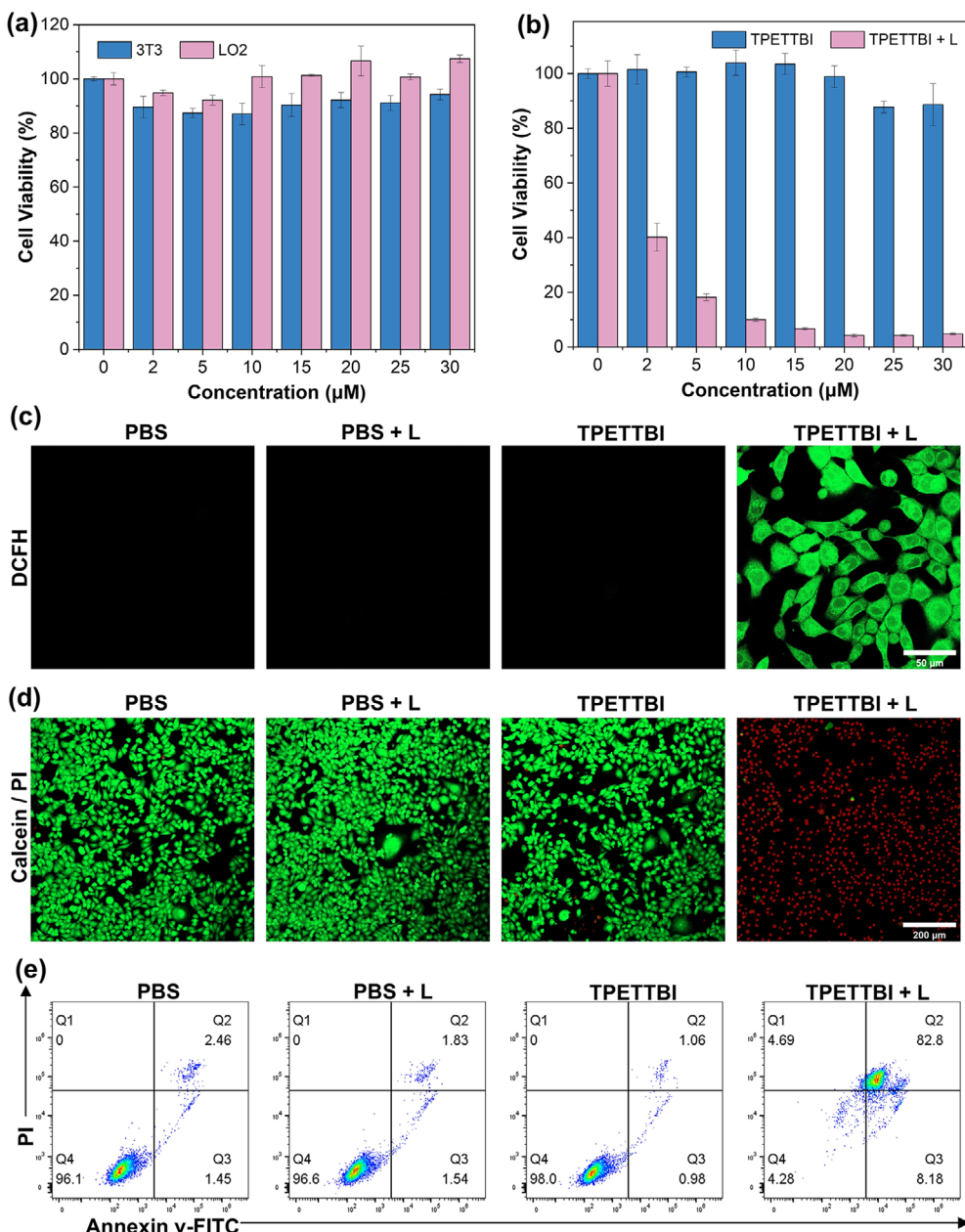


Figure 3. Anti-tumor property evaluation. a) dark toxicity and b) phototoxicity of TPETTBIs. c) Intracellular ROS detection using DCFH as an indicator. Scale bar = 50 μm . d) Live/dead staining assay for 4T1 cells under different conditions. Scale bar = 200 μm . e) FCM results of PI/Annexin v-FITC staining assay for 4T1 cells after different treatment.

assessed using CCK-8 assays. As shown in Figure 3a, even when incubated with 30 μM of TPETTBIs, the viability of 3T3 and LO2 cells remained above 90%, indicating negligible dark toxicity and good biocompatibility. Upon irradiation, the viability of 4T1 tumor cells decreased to 40% at a concentration as low as 2 μM (Figure 3b). Furthermore, intracellular ROS generation was evaluated using DCFH-DA (Figure 3c; Figure S16, Supporting Information). In contrast to other treatment groups, intense green fluorescence signals from DCF were observed in the group treated with TPETTBIs and 660 nm laser irradiation, indicating excess ROS generation within the cells. Subsequently, live/dead cell

staining was performed to validate the phototoxicity of TPETTBIs. As shown in Figure 3d and Figure S17 (Supporting Information), the group treated with TPETTBIs and 660 nm laser exhibited strong red signal, with only a few green signals observed, while other groups displayed predominantly green signal. Furthermore, the apoptosis rates of different treatment groups were evaluated by flow cytometry (FCM) (Figure 3e). Notably, the apoptosis rate of the group treated with TPETTBIs and laser increased to 82.8%, while the apoptosis rates of other groups remained below 5%, validating the low dark toxicity and good therapeutic efficacy of TPETTBIs.

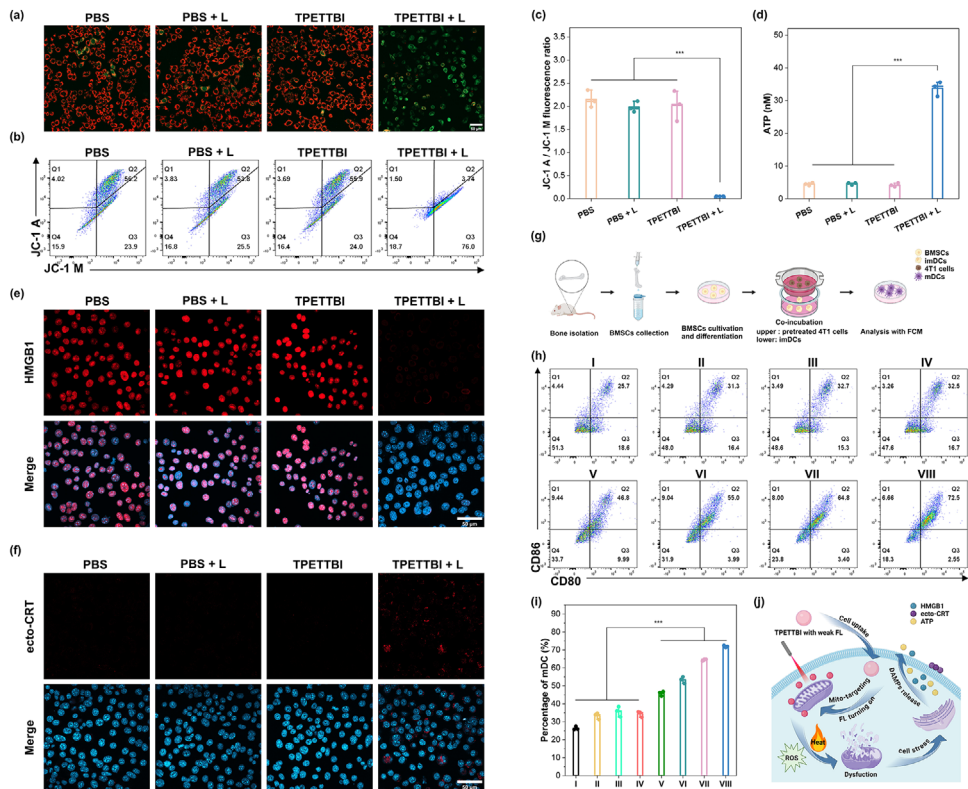


Figure 4. In vitro ICD induction mechanism of TPETTBI. a) CLSM images and b) FCM profiles of MMP changes after different treatments using JC-1 as indicator. Scale bar = 50 μ m. c) Corresponding quantitative analysis of the JC-1 A/JC-1 M ratio in the 4T1 cells after different treatments. d) Quantitative analysis of ATP levels. Immunofluorescence staining assay images of e) HMGB1, and f) ecto-CRT. g) Schematic illustration of the BMDCs maturation assay. Created in BioRender. <https://Biorender.com/owua05r>. h) FCM analysis of mature DCs (CD80⁺ CD86⁺, gated on CD11c⁺) and i) corresponding quantitative analysis. I = BMDC, II = PBS, III = PBS + L (15 min), IV = TPETTBI, V = TPETTBI + L (2 min), VI = TPETTBI + L (5 min), VII = TPETTBI + L (10 min), VIII = TPETTBI + L (15 min). j) Schematic illustration of the processes of ICD induction triggered by TPETTBI. Created in BioRender. <https://Biorender.com/p01m487>. The data presented as the mean \pm standard deviation ($n = 3$), *** $p < 0.001$.

2.5. Cellular ICD Induction Investigation

Given the excellent mitochondria-targeting capacity and therapeutic effect of TPETTBI, its impact on mitochondria was further investigated using JC-1 staining assays. JC-1 dye is commonly used to monitor changes in mitochondrial membrane potential (MMP) and typically exists in two forms within cells. In cells with high MMP, JC-1 emits strong red fluorescence. Conversely, a decrease in MMP leads to the formation of JC-1 monomers, resulting in a fluorescence shift from red to green, thus indicating MMP changes. As shown in Figure 4a, the group treated with TPETTBI and laser exhibited weak red fluorescence and relatively strong green fluorescence, resulting in green fluorescence in the merged image. In contrast, the other group predominantly displayed strong red fluorescence signals. The ratios of red to green fluorescence were also evaluated using FCM. As shown in Figure 4b,c, more than 75% of the cells emitted green fluorescence in the group treated with TPETTBI and laser, which was consistent with the JC-1 staining imaging results. These results suggest the dysfunction of mitochondria as a result of oxidative stress caused by PDT effect.

It has been established that ROS-induced mitochondrial stress can trigger large-scale ICD.^[25,27] Given the strong ROS generation, photothermal efficiency and excellent mitochondria-

targeting ability of TPETTBI, its potential for ICD induction was further evaluated. ICD induction is often accompanied by the release of damage-associated molecular patterns (DAMPs), such as adenosine triphosphate (ATP), high-mobility group box 1 (HMGB1) and surface-exposed CRT (ecto-CRT).^[11,42] Therefore, the level of ATP secretion was first studied. We observed that the concentration of ATP in the supernatant of 4T1 cells treated with TPETTBI and laser was significantly higher than those of the other three control groups (Figure 4d). Furthermore, immunofluorescence staining was performed to analyze the expression levels of HMGB1 and ecto-CRT in cells treated with different conditions. As shown in Figure 4e, negligible HMGB1 was observed in the group treated with TPETTBI and laser, indicating the migration and release of HMGB1. In the immunofluorescence staining for ecto-CRT (Figure 4f), the group treated with TPETTBI and laser exhibited intense red fluorescence signal of ecto-CRT on the cell surface, suggesting effective induction of ICD. These observations demonstrate that TPETTBI can effectively facilitate the generation and release of DAMPs, providing typical evidence of ICD occurrence caused by the synergistic effect of PDT and PTT.

The release of DAMPs can trigger a series of antitumor immune responses, including the recruitment of dendritic cells (DCs) and the promotion of DC maturation.^[43] To further confirm the release of DAMPs and the ICD effect induced by

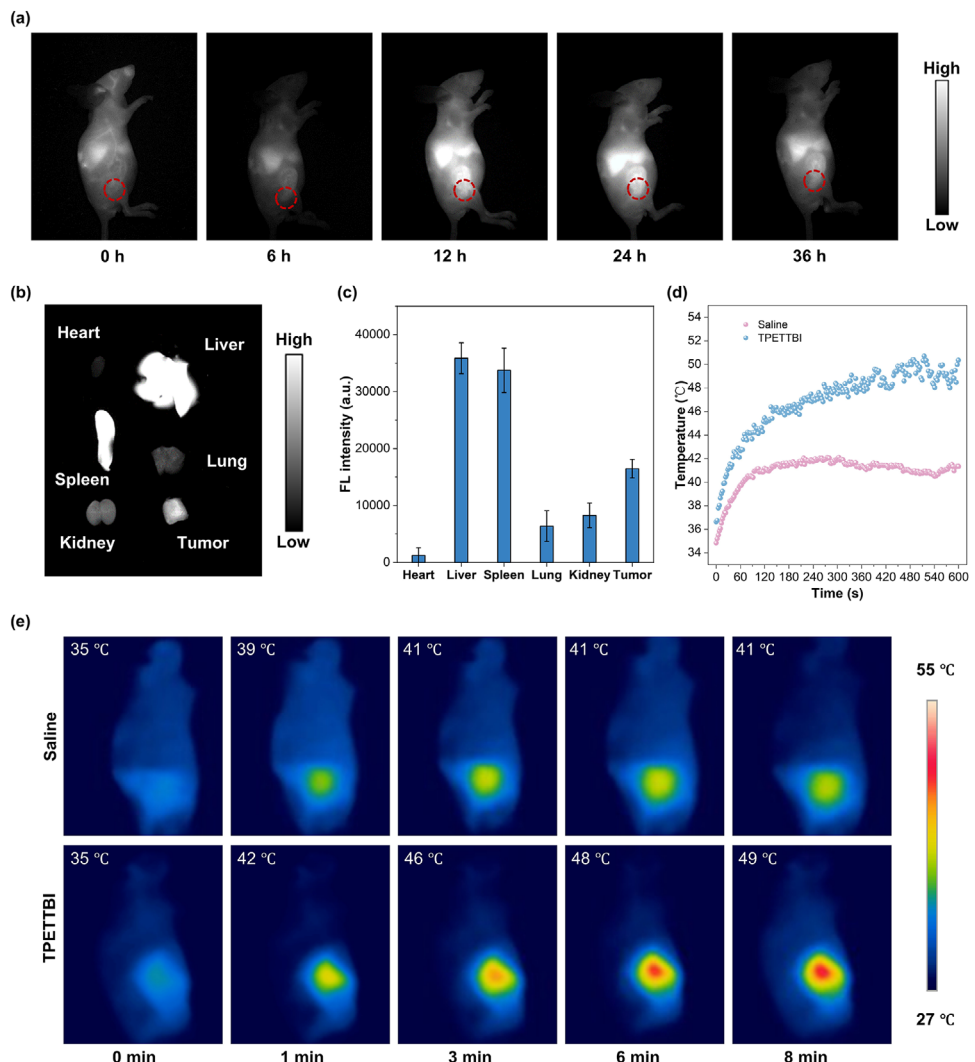


Figure 5. a) In vivo NIR-II fluorescence images of the 4T1 tumor-bearing mouse at different time points after intravenously treated with TPETTBI. b) Ex vivo NIR-II fluorescence images of tumors and different organs excised from 4T1 tumor-bearing mouse at 36 h postinjection. c) the corresponding fluorescence intensity quantitative analysis of tumors and different organs excised from 4T1 tumor-bearing mice at 36 h postinjection. In vivo d) photothermal profiles and e) photothermal images of 4T1 tumor-bearing mouse after intravenously treated with TPETTBI or saline.

TPETTBI, bone-marrow-derived dendritic cells (BMDCs) were isolated from 6-week-old BALB/C mice (Figure 4g). Subsequently, 4T1 cells were treated with different approaches and then co-cultured with BMDCs overnight. Finally, BMDCs were collected, and the expression of CD11c, CD80, and CD86, markers of mature DCs (mDCs), were analyzed using FCM. As demonstrated in Figure 4h,i, 4T1 cells pretreated with TPETTBI and laser irradiation caused a significant increase in the expression of CD80 and CD86 on BMDCs in an irradiation time-dependent manner, confirming light-triggered ICD induction and DAMP release. Collectively, these results indicate that TPETTBI can effectively accumulate in the mitochondria, where excessive ROS generated under irradiation causes mitochondrial dysfunction, promoting DAMP generation. Meanwhile, the photothermal effect facilitates the release of DAMPs, thus the synergistic PDT and PTT effects of TPETTBI can effectively induce large-scale ICD, and eventually leads to tumor cell death (Figure 4j).

2.6. In Vivo NIR-II Fluorescence Imaging and Photothermal Imaging

Encouraged by the positive results from in vitro experiment, in vivo performance of TPETTBI was then evaluated. TPETTBI was first encapsulated with DSPE-PEG2000, resulting in TPETTBI nanoparticles with a particle size of 147.8 nm and a zeta potential of -20.16 mV. These properties suggest good stability in biological environments (Figure S18, Supporting Information). Then the in vivo tumor imaging was first conducted in the 4T1 breast tumor-bearing mice model. As illustrated in Figure 5a, prior to the intravenous administration of TPETTBI, the mice displayed low fluorescence signal when observed through a long pass (LP) filter of 1050 nm, indicating minimal background interference. At 6 h post-injection, the NIR-II fluorescence signal on the tumor site could be captured by the NIR camera, which suggested successful accumulation of TPETTBI in the tumor tissue as a result

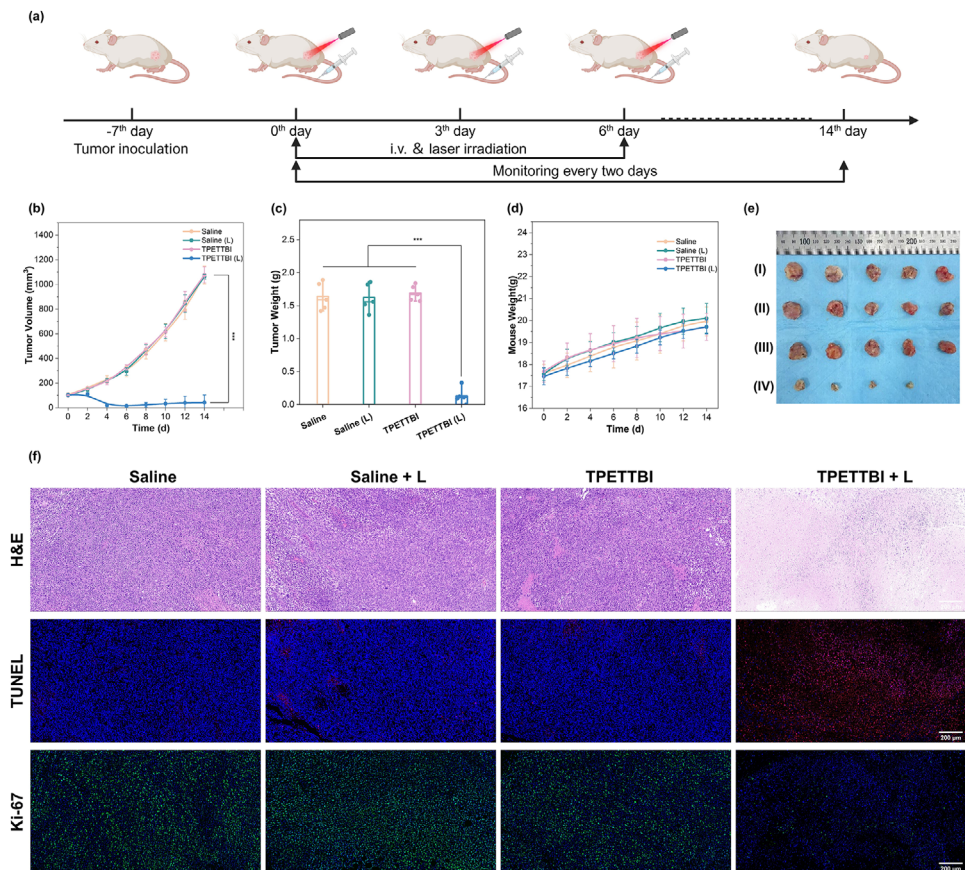


Figure 6. a) Schematic illustration of NIR-II FLI/PTI-guided phototherapeutic experiments. Created in BioRender. <https://Biorender.com/3fkibor>. b) Tumor volume growth curves during 14 days after different treatments. c) Tumor weight of the mice with different treatment at the end of 14-day treatment. d) Body weight of the mice during 14 days after different treatments. e) The photograph of the tumors excised from 4T1 tumor-bearing mice after different treatment for 14 days. I = PBS, II = PBS + L, III = TPETTBI, IV = TPETTBI + L. f) H&E, TUNEL, and Ki67 staining analysis of tumor tissues after various treatments. Scale bar = 200 μ m. The data presented as the mean \pm standard deviation ($n = 5$), *** $p < 0.001$.

of enhanced permeability and retention (EPR) effect. The fluorescence signal at the tumor site gradually enhanced and reached its maximum at 12 h post-injection, then started to decay because of metabolism. Additionally, ex vivo fluorescence analysis of the tumor tissue at 36 h post-injection verified the effective accumulation of TPETTBI (Figure 5b,c). Given that the TPETTBI showed excellent photothermal conversion capacity, we further evaluated it's in vivo photothermal effect using infrared thermal camera. As shown in Figure 5d,e, the temperature at the tumor site quickly increased from 35 to 49 °C upon exposure to a 660 nm laser (0.4 W cm^{-2}) for 8 min at 12 h post-injection. In contrast, the mice treated with saline only exhibited a negligible temperature change. Collectively, the results from NIR-II fluorescence imagining and IR thermal imagining demonstrate that TPETTBI holds great potential in ultrasensitive tumor imagining and effective in vivo tumor therapy.

2.7. Synergistic Phototherapy of Tumor In Vivo

Subsequently, the in vivo antitumor properties of TPETTBI were evaluated using a 4T1 tumor-bearing BALB/c mouse model (Figure 6a). Specifically, 4T1 tumor-bearing mice were randomly

divided into four groups: two control groups treated with saline, with or without laser irradiation, one control group treated with TPETTBI alone, and one experimental group treated with TPETTBI followed by 660 nm laser irradiation at 12 h post-injection. As shown in Figure 6b,e, by the end of the 14-day treatment period, the tumor volumes in the three control groups increased rapidly, whereas the tumor volume in the group treated with TPETTBI and laser irradiation significantly decreased. Meanwhile, the tumor weights in the group treated with TPETTBI and laser irradiation significantly decreased by the end of the treatment (Figure 6c), indicating an effective light-triggered antitumor effect in the mouse model. Additionally, the body weights of mice in all four groups showed no significant differences (Figure 6d), suggesting good biosafety during the experiment. The extensive destruction and suppression of cell proliferation in the tumor tissue, caused by the combined effects of PDT and PTT, were further confirmed by hematoxylin and eosin (H&E) staining, terminal deoxynucleotidyl transferase dUTP nick-end labeling (TUNEL) staining, and Ki67 immunofluorescence staining (Figure 6f). Furthermore, H&E staining of the main organs from mice in the phototherapy experiment revealed no pathological damage, reinforcing the excellent biological safety of TPETTBI (Figure S19, Supporting Information). Additionally, orbital

blood samples were collected at the end of the treatment to evaluate potential liver and renal function abnormalities (Figure S20, Supporting Information). The results showed no significant differences between the experimental group and the three control groups, confirming the excellent biocompatibility of TPETTBI. The results of hemolysis assays further supported the favorable safety profile of TPETTBI for *in vivo* experiments (Figure S21, Supporting Information). Taken together, these results indicate that TPETTBI could effectively inhibit tumor growth with negligible toxicity via NIR-II fluorescence imaging-guided synergistic effects of PDT and PTT.

2.8. Photoimmunotherapy Evaluation on Bilateral Tumor-Bearing Model

Motivated by the promising NIR-II imaging ability and excellent phototherapy efficacy of TPETTBI *in vivo*, we further investigated its potential to induce immunogenic cell death (ICD) within a bilateral 4T1 tumor-bearing mouse model. As illustrated in Figure 7a, each BALB/c mouse was first inoculated with a primary tumor, followed by a secondary tumor inoculation three days later to simulate the presence of metastatic tumor. Seven days after the initial tumor inoculation, all 4T1 tumor-bearing mice with both primary and distant tumors were randomly divided into four groups: Saline, Saline + Laser, TPETTBI and TPETTBI + Laser. The mice in these groups received treatment on days 0, 3, and 6, respectively, with only the primary tumors subjected to laser irradiation at 12 h post-injection in the laser groups. As shown in Figure 7b–e and Figure S22 (Supporting Information), after 21 days of treatment, the group treated with TPETTBI and laser irradiation exhibited significant inhibition of tumor growth in both the primary and distant tumors. In contrast, the “Saline”, “Saline + Laser”, and “TPETTBI-only” groups showed no significant suppression of bilateral tumor growth. Importantly, no treatments resulted in significant changes in the body weight of the mice. These results suggest TPETTBI possesses light-trigger antitumor immune activation capability.

To elucidate the mechanisms underlying TPETTBI’s superior antitumor efficacy, immune cell responses in the spleens and metastatic tumors of treated mice were assessed. First, we evaluated the maturation of DCs in the spleens of mice by FCM (Figure 7f,g; Figure S23, Supporting Information). Notably, we observed that the proportion of mature dendritic cells (CD11C⁺ CD80⁺ CD86⁺) in the spleens of mice in the “TPETTBI + Laser” group was significantly higher than in the other groups, indicating successful DC maturation induced by TPETTBI and laser irradiation. Given that mature dendritic cells (mDCs) play a critical role in tumor antigen presentation, which facilitates the proliferation and activation of T lymphocytes,^[43,44] we further analyzed T lymphocytes in spleen tissues (Figure 7h,i; Figure S24, Supporting Information). As expected, the percentage of CD4⁺ and CD8⁺ T cells was significantly higher in the spleens of mice treated with TPETTBI and laser irradiation, likely due to the increased number of mDCs. The infiltration of activated T cells is essential for effective antitumor immunotherapy.^[9,45,46] Therefore, we also assessed activated T cells in the metastatic tumors to evaluate the immunological effects on the untreated tumor (Figure 7j–m). Flow cytometry results demonstrated that TPETTBI and laser ir-

radiation on the primary tumor effectively promoted the infiltration of activated T cells into the untreated metastatic tumor, which was further confirmed by immunofluorescence staining. Taken together, these results demonstrate that TPETTBI, as a mitochondria-targeting AIEgen with superior ROS generation and photothermal efficiency, can elicit strong antitumor immunity by inducing large-scale immunogenic cell death.

3. Conclusion

In summary, we present a novel molecular design strategy that integrates the characteristics of AIE, NIR emission, mitochondria targeting, superior ROS generation, and high photothermal conversion into a single molecule, aiming at achieving tumor eradication through large-scale ICD induction. Specifically, through rational molecular engineering, we endowed TPETTBI with a twisted structure, amphiphilic property and enhanced D-A strength, which resulted in excellent mitochondria targeting, efficient ROS generation and high photothermal conversion. *In vitro* imaging results confirmed the mitochondria-targeting ability and turn-on fluorescence of TPETTBI. Both *in vitro* and *in vivo* antitumor studies demonstrated that TPETTBI not only could serve as a phototherapy agent with NIR-II fluorescence monitoring capability, but also could act as an efficient ICD inducer. The synergistic PDT and PTT effects on the specific organelle within the biological tissue transparency window facilitated effective and precise tumor eradication, as well as enhanced ICD induction. This study provides new perspectives on the rational design of powerful phototherapy agents for targeted and effective tumor treatment by incorporating synergistic PDT, PTT, and ICD-based immunotherapy into a single molecule.

4. Experimental Section

Materials: All starting materials were purchased from Bidepharm, and Energy. 2',7'-dichlorodihydrofluorescein diacetate (DCFH-DA), 9,10-anthracenediyi-bis(methylene) dimalonic acid (ABDA), dihydrorhodamine 123 (DHR123), chlorin e6 (Ce6) were obtained from Bidepharm (Shanghai, China). Rose Bengal (RB) was obtained from Sigma-Aldrich (USA). Dulbecco’s modified Eagle’s medium (DMEM) and RPMI 1640 culture medium were obtained from Gibco (Life Technologies). Fetal bovine serum (FBS) was sourced from Procell. Mito-Tracker Green, Lysotracker Green, DiO, mitochondrial membrane potential assay kit (JC-1), Calcein-AM/PI, live/dead cell staining kit, Alexa Fluor 647-labeled Goat Anti-Rabbit IgG(H+L), Enhanced ATP Assay Kit and cell counting kit-8 (CCK-8) were obtained from Beyotime Biotech (Shanghai, China). Recombinant murine GM-CSF and IL-4 were sourced from PeproTech (USA). Recombinant Anti-Calreticulin antibody and Anti-High Mobility Group Box 1 antibody were obtained from Abcam (USA). FITC anti-mouse CD11c antibody, PE anti-mouse CD80 antibody, APC anti-mouse CD86 antibody, FITC anti-mouse CD3e antibody, Brilliant Violet 421 anti-mouse CD4, APC anti-mouse CD8a and TruStain FcX PLUS (anti-mouse CD16/32) were obtained from biogend (USA). Ultrapure water (>18 MΩ·cm) from a Milli-Q reference system (Millipore) was used throughout. All other reagents and solvents were used directly without further purification.

Cell Culture: 4T1 cells were cultured in RPMI 1640 medium. NIH 3T3 cells and LO2 cells were cultured in DMEM. All medium containing 10% FBS and 1% PS (100 units mL⁻¹ penicillin and 100 mg mL⁻¹ streptomycin). Cells were incubated in a standard incubator, maintained at 37 °C, 5% CO₂.

Tumor Model Establishment: All experimental protocols and ethical reviews related to animal experiments have been approved by the

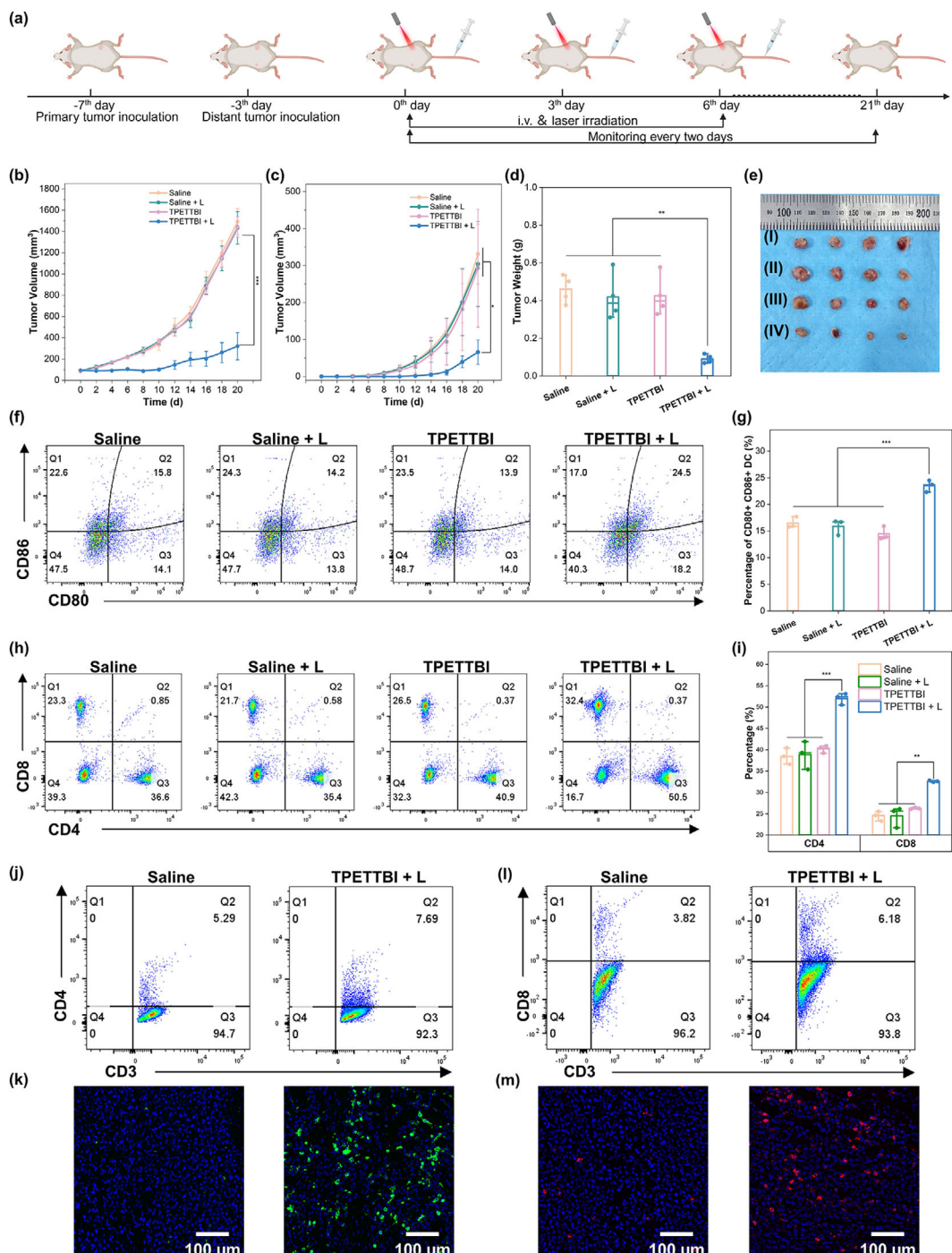


Figure 7. a) Schematic illustration of NIR-II FLI/PTI-guided phototherapeutic experiments on a bilateral 4T1 tumor-bearing mouse model. Created in BioRender. <https://Biorender.com50mduvy>. b) Primary and c) distant tumor volume growth curves during 21 days after different treatments. d) Distant tumor weight of the mice with different treatment at the end of 21-day treatment. e) The photograph of distant tumors excised from bilateral 4T1 tumor-bearing mice after different treatment for 21 days. I = PBS, II = PBS + L, III = TPETTBI, IV = TPETTBI + L. f) FCM profiles and g) corresponding quantitative analysis of mature DCs ($CD80^+ CD86^+$, gated on $CD11c^+$) in the spleen tissue form the mice with different treatments. h) FCM profiles and i) corresponding quantitative analysis of $CD4^+$ and $CD8^+$ T cells (gated on $CD3^+$) in the spleen tissue form the mice with different treatments. j) FCM profiles and k) immunofluorescence images of $CD4^+$ T cells in the distant tumor tissue of bilateral 4T1 tumor-bearing mice form “Saline” group and “TPETTBI + L” group. Scale bar = 100 μ m. l) FCM profiles and m) immunofluorescence images of $CD8^+$ T cells in the distant tumor tissue of bilateral 4T1 tumor-bearing mice form “Saline” group and “TPETTBI + L” group. Scale bar = 100 μ m. The data presented as the mean \pm standard deviation ($n = 4$ for (b), (c), and (d), $n = 3$ for (g) and (i)), * $p < 0.05$, ** $p < 0.01$, *** $p < 0.001$.

Experimental Animal Ethics Review Committee of Southern Medical University (SMUL2022257). The tumor models were established by subcutaneous injection of 4T1 cells (1×10^6).

Statistical Analysis: Data were shown as mean \pm standard deviation (S.D.). Statistical differences between two groups were assessed using Student's *t*-test, while comparisons among multiple groups were conducted using one-way ANOVA followed by Tukey's post-hoc test. Statistical analysis was conducted using Origin software. A *p*-value of less than 0.05 was deemed statistically significant, while "n.s." indicates no significant difference. (*, **, and *** indicate $p < 0.05$, $p < 0.01$, and $p < 0.001$, respectively).

Supporting Information

Supporting Information is available from the Wiley Online Library or from the author.

Acknowledgements

L.Y. and J.H. contributed equally to this work. This work was financially supported by the National Natural Science Foundation of China (22205096, 22101028 and 22205025), the Outstanding Youths Development Scheme of Nanfang Hospital, Southern Medical University (2024J011), National Key R&D Program of China (2022YFE0140400), Guangdong Basic and Applied Basic Research Foundation (2023A1515011924 and 2025A1515010638), Science and Technology Program of Guangzhou (2025A04J7221), Guangdong Provincial Pearl River Talents Program (2021QN02Y116), the start-up funding from Beijing Normal University (310432102, 310432103), and the Innovation and Technology Commission of Hong Kong (ITC-CNERC14SC01 and ITCPD/17-9).

Conflict of Interest

The authors declare no conflict of interest.

Data Availability Statement

The data that support the findings of this study are available from the corresponding author upon reasonable request.

Keywords

aggregation-induced emission, immunogenic cell death, photoimmunotherapy

Received: January 29, 2025

Revised: March 25, 2025

Published online: April 21, 2025

- [1] R. L. Siegel, A. N. Giaquinto, A. Jemal, *CA Cancer J. Clin.* **2024**, *74*, 12.
- [2] A. G. Arranja, V. Pathak, T. Lammers, Y. Shi, *Pharmacol. Res.* **2017**, *115*, 87.
- [3] X. Guo, N. Yang, W. Ji, H. Zhang, X. Dong, Z. Zhou, L. Li, H.-M. Shen, S. Q. Yao, W. Huang, *Adv. Mater.* **2021**, *33*, 2007778.
- [4] B. Zhou, J. Liu, M. Lin, J. Zhu, W. R. Chen, *Coord. Chem. Rev.* **2021**, *442*, 214009.
- [5] Y. Wang, M. Wang, H.-X. Wu, R.-H. Xu, *Cancer Commun.* **2021**, *41*, 803.
- [6] O. K. Dagher, R. D. Schwab, S. K. Brookens, A. D. Posey, *Cell* **2023**, *186*, 1814.

- [7] M. He, M. Xiao, R. Wang, J. Fan, X. Peng, W. Sun, *Prog. Mater. Sci.* **2025**, *147*, 101347.
- [8] B. Wu, B. Zhang, B. Li, H. Wu, M. Jiang, *Signal Transduction Targeted Ther.* **2024**, *9*, 274.
- [9] T. F. Gajewski, H. Schreiber, Y.-X. Fu, *Nat. Immunol.* **2013**, *14*, 1014.
- [10] G. Kroemer, C. Galassi, L. Zitvogel, L. Galluzzi, *Nat. Immunol.* **2022**, *23*, 487.
- [11] D. V. Krysko, A. D. Garg, A. Kaczmarek, O. Krysko, P. Agostinis, P. Vandenberghe, *Nat. Rev. Cancer* **2012**, *12*, 860.
- [12] M. Chen, Y. Sun, H. Liu, *Interdiscipl. Med.* **2023**, *1*, 20220012.
- [13] N. Feng, Z. Peng, X. Zhang, Y. Lin, L. Hu, L. Zheng, B. Z. Tang, J. Zhang, *Nat. Commun.* **2024**, *15*, 8187.
- [14] X. Duan, C. Chan, W. Lin, *Angew. Chem., Int. Ed.* **2019**, *58*, 670.
- [15] Y. Sun, Y. Hu, Y. Geng, C. Wan, Y. Liu, Y. Liao, X. Shi, J. F. Lovell, K. Yang, H. Jin, *Exploration* **2024**, *4*, 20220170.
- [16] Y. Li, Y. Duan, Y. Li, Y. Gu, L. Zhou, Z. Xiao, X. Yu, Y. Cai, E. Cheng, Q. Liu, Y. Jiang, Q. Yang, F. Zhang, Q. Lei, B. Yang, *Exploration* **2025**, *5*, 20230117.
- [17] Y. Wang, K. Ma, M. Kang, D. Yan, N. Niu, S. Yan, P. Sun, L. Zhang, L. Sun, D. Wang, H. Tan, B. Z. Tang, *Chem. Soc. Rev.* **2024**, *53*, 12014.
- [18] Y. Yu, H. Wang, Z. Zhuang, C. Ji, L. Zhang, Y. Li, Z. Zhao, D. Ding, G. Feng, B. Z. Tang, *ACS Nano* **2024**, *18*, 13019.
- [19] B. C. Wilson, R. A. Weersink, *Photochem. Photobiol.* **2020**, *96*, 219.
- [20] A. P. Castano, T. N. Demidova, M. R. Hamblin, *Photodiagnosis Photodyn. Ther.* **2005**, *2*, 1.
- [21] S. S. Liew, X. Qin, J. Zhou, L. Li, W. Huang, S. Q. Yao, *Angew. Chem., Int. Ed.* **2021**, *60*, 2232.
- [22] N. Gong, X. Ma, X. Ye, Q. Zhou, X. Chen, X. Tan, S. Yao, S. Huo, T. Zhang, S. Chen, X. Teng, X. Hu, J. Yu, Y. Gan, H. Jiang, J. Li, X.-J. Liang, *Nat. Nanotechnol.* **2019**, *14*, 379.
- [23] K. Qian, S. Gao, Z. Jiang, Q. Ding, Z. Cheng, *Exploration* **2024**, *4*, 20230063.
- [24] J. Zielonka, J. Joseph, A. Sikora, M. Hardy, O. Ouari, J. Vasquez-Vivar, G. Cheng, M. Lopez, B. Kalyanaraman, *Chem. Rev.* **2017**, *117*, 10043.
- [25] X. Wang, J. Qian, Z. Yang, Y. Song, W. Pan, Y. Ye, X. Qin, X. Yan, X. Huang, X. Wang, M. Gao, Y. Zhang, *Adv. Mater.* **2024**, *36*, 2310964.
- [26] F. Lin, Y.-W. Bao, F.-G. Wu, *Molecules* **2018**, *23*, 3016.
- [27] C. Chen, X. Ni, S. Jia, Y. Liang, X. Wu, D. Kong, D. Ding, *Adv. Mater.* **2019**, *31*, 1904914.
- [28] J.-F. Yu, Y. Wen, M. Li, *Adv. Funct. Mater.* **2024**, *34*, 2402663.
- [29] J. Mei, N. L. C. Leung, R. T. K. Kwok, J. W. Y. Lam, B. Z. Tang, *Chem. Rev.* **2015**, *115*, 11718.
- [30] Z. Ye, W. He, Z. Zhang, Z. Qiu, Z. Zhao, B. Z. Tang, *Interdiscip. Med.* **2023**, *1*, 20220011.
- [31] X.-Y. Wang, J. Gong, H. Zou, S. H. Liu, J. Zhang, *Aggregate* **2023**, *4*, 252.
- [32] B. He, J. Huang, J. Zhang, H. H. Y. Sung, J. W. Y. Lam, Z. Zhang, S. Yan, D. Wang, J. Zhang, B. Z. Tang, *Angew. Chem., Int. Ed.* **2022**, *61*, 202117709.
- [33] Y. Liao, Z. Peng, X. Liu, Y. Hu, J. Zhang, *Interdiscip. Med.* **2023**, *1*, 20230024.
- [34] P. Cen, J. Huang, C. Jin, J. Wang, Y. Wei, H. Zhang, M. Tian, *Aggregate* **2023**, *4*, 352.
- [35] F. Hu, S. Xu, B. Liu, *Adv. Mater.* **2018**, *30*, 1801350.
- [36] W. Fan, P. Huang, X. Chen, *Chem. Soc. Rev.* **2016**, *45*, 6488.
- [37] S. Jia, Z. Gao, Z. Wu, H. Gao, H. Wang, H. Ou, D. Ding, *CCS Chem.* **2021**, *4*, 501.
- [38] C. Li, G. Chen, Y. Zhang, F. Wu, Q. Wang, *J. Am. Chem. Soc.* **2020**, *142*, 14789.
- [39] Z. Feng, S. Bai, J. Qi, C. Sun, Y. Zhang, X. Yu, H. Ni, D. Wu, X. Fan, D. Xue, S. Liu, M. Chen, J. Gong, P. Wei, M. He, J. W. Y. Lam, X. Li, B. Z. Tang, L. Gao, J. Qian, *Adv. Mater.* **2021**, *33*, 2008123.
- [40] C. Ou, L. An, Z. Zhao, F. Gao, L. Zheng, C. Xu, K. Zhang, J. Shao, L. Xie, X. Dong, *Aggregate* **2023**, *4*, 290.

- [41] Z. Zhao, H. Zhang, J. W. Y. Lam, B. Z. Tang, *Angew. Chem., Int. Ed.* **2020**, *59*, 9888.
- [42] Z. Gao, S. Jia, H. Ou, Y. Hong, K. Shan, X. Kong, Z. Wang, G. Feng, D. Ding, *Angew. Chem., Int. Ed.* **2022**, *61*, 202209793.
- [43] E. Ascic, F. Åkerström, M. Sreekumar Nair, A. Rosa, I. Kurochkin, O. Zimmermannova, X. Catena, N. Rotankova, C. Veser, M. Rudnik, T. Ballocci, T. Schärer, X. Huang, M. de Rosa Torres, E. Renaud, M. Velasco Santiago, Ö. Met, D. Askmyr, M. Lindstedt, L. Greiff, L.-A. Ligeon, I. Agarkova, I. M. Svane, C. F. Pires, F. F. Rosa, C.-F. Pereira, *Science* **2024**, *386*, adn9083.
- [44] H. Cao, H. Gao, L. Wang, Y. Cheng, X. Wu, X. Shen, H. Wang, Z. Wang, P. Zhan, J. Liu, Z. Li, D. Kong, Y. Shi, D. Ding, Y. Wang, *ACS Nano* **2022**, *16*, 13992.
- [45] X. Kang, Y. Zhang, J. Song, L. Wang, W. Li, J. Qi, B. Z. Tang, *Nat. Commun.* **2023**, *14*, 5216.
- [46] Z. Liu, J. Zhang, H. Liu, H. Shen, N. Meng, X. Qi, K. Ding, J. Song, R. Fu, D. Ding, G. Feng, *Adv. Mater.* **2023**, *35*, 2208692.